

Topology of Entanglement Evolution of Two Qubits

Dong Zhou, Gia-Wei Chern, Jianjia Fei, and Robert Joynt

Physics Department, University of Wisconsin-Madison, Madison, Wisconsin 53706, USA

(Dated: February 5, 2022)

The dynamics of a two-qubit system is considered with the aim of a general categorization of the different ways in which entanglement can disappear in the course of the evolution, e.g., entanglement sudden death. The dynamics is described by the function $\vec{n}(t)$, where \vec{n} is the 15-dimensional polarization vector. This representation is particularly useful because the components of \vec{n} are direct physical observables, there is a meaningful notion of orthogonality, and the concurrence C can be computed for any point in the space. We analyze the topology of the space S of separable states (those having $C = 0$), and the often lower-dimensional linear dynamical subspace D that is characteristic of a specific physical model. This allows us to give a rigorous characterization of the four possible kinds of entanglement evolution. Which evolution is realized depends on the dimensionality of D and of $D \cap S$, the position of the asymptotic point of the evolution, and whether or not the evolution is “distance-Markovian”, a notion we define. We give several examples to illustrate the general principles, and to give a method to compute critical points. We construct a model that shows all four behaviors.

PACS numbers: 02.40.Pc, 03.65.Ud, 03.65.Yz, 03.67.Mn

I. INTRODUCTION

Entanglement is one of the most intriguing aspects of quantum physics and is known to be a useful resource for quantum computation and communication [1, 2]. However, its structure and evolution in time are not fully understood even for simple systems such as two qubits where a relatively computable entanglement measure, the Wootters’ concurrence C , is available [3]. The difficulty resides in the high dimensionality of state spaces (fifteen for two qubits) and the non-analyticity of the definition of the entanglement measure C .

In the presence of external noise, pure states become mixed and entanglement degrades. These are distinct but related issues. The completely mixed state (density matrix proportional to the unit matrix) is separable: it has $C = 0$. Pure states, on the other hand, can have any value of C between 0 and 1 inclusive. Purity (measured, for example, by the von Neumann entropy) tends to decrease monotonically and smoothly with time under Markovian evolution. The same is not true for entanglement. Apart from the expected smooth half-life (HL) decaying behavior, the sudden disappearance of entanglement has been theoretically predicted and experimentally observed [4, 5]. Widely known as entanglement sudden death (ESD), this non-analytic behavior has been shown to be a generic feature of multipartite quantum systems regardless of whether the environment is modeled as quantum or classical [6–19]. While the monotonic decrease of $C(t)$ is usually associated with Markovian evolution, non-Markovian evolution can also lead to entanglement sudden birth (ESB). It is believed to be related to the memory effect of the (non-Markovian) environment [6, 18–21]. Although most investigations have been focused on two-qubit systems and we will also focus on this case, ESD and ESB have been shown to exist in multi-qubit systems, and even in quantum systems with

infinite dimensional Hilbert spaces, such as harmonic oscillators [22–28].

Our aim in this paper is to formulate the problem of the evolution of entanglement in two-qubit systems in the polarization vector space, and to show that this formulation leads naturally to a categorization of entanglement evolutions into four distinct types, generalizing and making precise the concepts of HL, ESD, and ESB behaviors. It turns out that these categories are consequences of certain topological characteristics of a model. To show this, we proceed as follows. Sec. II characterizes in detail two manifolds in the polarization vector space: the manifold of admissible physical states and the manifold of separable states. Sec. III presents the concept of a dynamical subspace - a manifold that is associated with a physical model, and then gives several concrete examples of models of increasing complexity. In Sec. III we also show how to compute critical points: parameter values that separate one behavior from another. In Sec. IV, we prove that our categorization scheme is exhaustive. Sec. V presents the final results and discussion.

II. ENTANGLEMENT IN POLARIZATION VECTOR SPACE

The universality of the various entanglement behaviors suggests that they are derived from some structural property of entanglement in the physical state space, and that the system dynamics can be viewed as a probe of that property. To state this property precisely, we need to first characterize the space of all admissible density matrices ρ , or equivalently, the space of all admissible polarization vectors.

For two qubits, the polarization vector $\vec{n} =$

$(n_1, n_2, \dots, n_{15})$ is defined by the equation

$$\rho = \frac{1}{4}I_4 + \frac{1}{4}\sum_{i=1}^{15}n_i\mu_i, \quad (1)$$

where I_4 is the 4×4 unit matrix and the μ_i are the generators of $SU(4)$, satisfying

$$\mu_i = \mu_i^\dagger, \quad \text{Tr } \mu_i = 0, \quad \text{Tr } \mu_i \mu_j = 4\delta_{ij}. \quad (2)$$

For our purposes the μ_i are most conveniently chosen as

$$\mu_{\alpha\beta} = \sigma_\alpha \otimes \sigma_\beta, \quad (3)$$

where σ_α acts on the first qubit and σ_β acts on the second qubit. α and β sum over the 2×2 unit matrix I and the Pauli matrices X , Y and Z . Thus, in Eqs. 1 and 2, i is regarded as a composite index of α and β , but the $\sigma_\alpha = \sigma_\beta = I$ term is singled out. This space has the usual Euclidean inner product (which corresponds to the Hilbert-Schmidt inner product on the density matrices), and the inner product induces a metric and a topology in the usual fashion. The components of \vec{n} are physical observables and can be calculated by $n_i = \text{Tr } \rho \mu_i$. For example, the average value of the z -component of the spin of the first qubit is $\langle Z \otimes I \rangle = \text{Tr } [\rho(Z \otimes I)] = n_{ZI}$. The six components n_{IX} , n_{IY} , n_{IZ} , n_{XI} , n_{YI} and n_{ZI} represent physical polarizations of spin qubits. The other nine components (n_{XX} , etc.) are inter-qubit correlation functions. The most common name for \vec{n} is ‘‘polarization vector’’, but ‘‘coherence vector’’ and ‘‘generalized Bloch vector’’ are also in use. We note that different normalizations in Eqs. 1 and 2 are used in the literature [29–33].

The generators μ_i satisfy

$$\mu_i \mu_j = \delta_{ij}I + (if_{ijk} + d_{ijk})\mu_k \quad (4)$$

where f_{ijk} is totally anti-symmetric and d_{ijk} is totally symmetric. These structure constants can be found in Appendix A.

Eq. 1 holds for a 4-level system. It has an obvious generalization to N -level systems; the μ_i just become the $N^2 - 1$ generators of $SU(N)$. For $N = 2$, \vec{n} is the usual Bloch vector in a real 3-dimensional vector space. It is important to stress that the correspondence between ρ and \vec{n} is one-to-one; they give completely equivalent descriptions of the physical system. Certain physical concepts have geometric interpretations when stated in terms of \vec{n} ; as we shall see below. This is not so true of ρ . In our opinion, \vec{n} is the more convenient quantity for most purposes. ρ has been the traditional language in which to describe mixed states, but some experimental groups now favor \vec{n} [34, 35].

We shall refer to the set of all admissible \vec{n} as M , the state space. What shape does M have? Eq. 1 guarantees that ρ is Hermitian and has unit trace. To guarantee that ρ is positive (all its eigenvalues are non-negative), we also need the condition that all coefficients a_i of the characteristic polynomial $\det(xI_N - \rho) = \sum_{j=0}^N (-1)^j a_j x^{N-j}$ are non-negative [36]. Note $a_0 = 1$ by definition.

For two-qubit systems there are four of them, which are

$$1!a_1 = \text{Tr } \rho = 1, \quad (5)$$

$$2!a_2 = 1 - \text{Tr } \rho^2, \quad (6)$$

$$3!a_3 = 1 - 3\text{Tr } \rho^2 + 2\text{Tr } \rho^3, \quad (7)$$

$$4!a_4 = 1 - 6\text{Tr } \rho^2 + 8\text{Tr } \rho^3 + 3(\text{Tr } \rho^2)^2 - 6\text{Tr } \rho^4. \quad (8)$$

Note that $a_1 \geq 0$ is trivially satisfied for all density matrices.

For one qubit $N = 2$, \vec{n} is the usual Bloch vector, and only the $a_2 \geq 0$ constraint applies. Thus the positivity requirement is that $|\vec{n}| \leq 1$ and M is the familiar 3-dimensional spherical volume. For the 2-qubit $N = 4$ case that we are concerned with, there are cubic and quadratic inequalities to be satisfied, so the surface that bounds M is not so simple. The main point, however, is that M is convex: the line joining any two points in M is also in M . This follows from the convexity argument for ρ : if ρ_1 and ρ_2 are positive, then so is $s\rho_1 + (1-s)\rho_2$ for all $0 \leq s \leq 1$. This argument clearly also holds for \vec{n} .

All of the positivity requirements can be written in terms of \vec{n} , but the higher-order ones are fairly complicated. The requirement $1 - \text{Tr } \rho^2 \geq 0$ is of particular interest, since it has a simple expression in terms of \vec{n} :

$$\begin{aligned} 0 &\leq 1 - \text{Tr } (\rho^2) \\ &= 1 - \frac{1}{16} \left[\text{Tr } I_4 + 2 \sum_i^{15} n_i \text{Tr } \mu_i + \sum_{i,j=1}^{15} n_i n_j \text{Tr } \mu_i \mu_j \right] \\ &= \frac{3}{4} - \frac{1}{4} |\vec{n}|^2, \quad \text{or } |\vec{n}|^2 \leq 3. \end{aligned}$$

Hence the vectors in M lie within a sphere of radius $\sqrt{3}$. Technically, M is a 15-dimensional manifold with boundary. We will follow physics usage and also employ the term ‘‘space’’ for M , though of course it is not closed under vector addition. Note that pure states satisfy $\text{Tr } \rho^2 = 1$, so the pure states are a subset of the 14-sphere in M with $|\vec{n}| = \sqrt{3}$. To be more specific, the two-qubit pure states $|\psi\rangle\langle\psi|$ are of measure zero on that sphere since they can be parametrized by 6 real parameters

$$\begin{aligned} |\psi\rangle &= \cos\theta_1|00\rangle + e^{i\phi_1} \sin\theta_1 \sin\theta_2|01\rangle \\ &\quad + e^{i\phi_2} \sin\theta_1 \cos\theta_2 \cos\theta_3|10\rangle \\ &\quad + e^{i\phi_3} \sin\theta_1 \cos\theta_2 \sin\theta_3|11\rangle. \end{aligned}$$

An overall phase has been dropped in writing $|\psi\rangle$ since it does not appear in ρ .

Further insight into the shape of M can be gained by noting that M must be invariant under local unitary transformations (rotations of one spin at a time), which means that M has cylindrical symmetry around the 6 single-qubit axes. This is verified by making some 2-dimensional sections of M with exactly two components of \vec{n} non-zero. In contrast to Ref. [37] where a different basis was used (generalized Gell-Mann matrices), we find

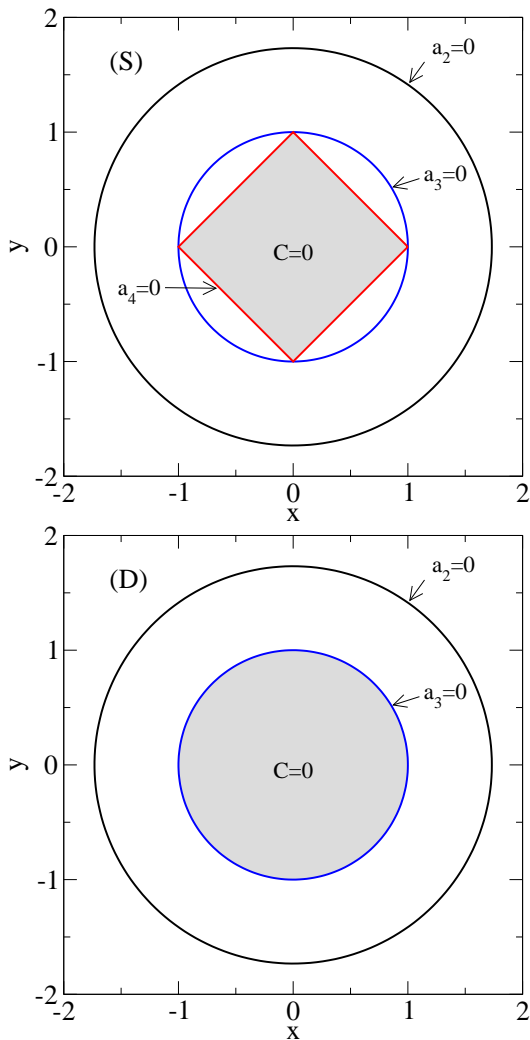


FIG. 1. (Color online) Two dimensional sections of the full two-qubit state space M , keeping only two components of the polarization vector non-zero. Only two inequivalent sections are possible: the disc section (D) and square section (S). The physical states are colored grey. $a_2 = 0$ is outlined as black, $a_3 = 0$ blue and $a_4 = 0$ red. All physical states in these two dimensional section are separable states.

only two types of shapes, as shown in Fig. 1 and tabulated in Table I. Using the structure constants d_{ijk} and f_{ijk} , it can be shown that the square and disc sections are the only possibilities along the $n_i - n_j$ plane. When μ_i commutes with μ_j the section is a square and μ_i anti-commutes with μ_j the section is a circular disc. Details can be found in Appendix A.

The discs correspond to the local rotations between single-qubit-type axes, such as the $n_{IX} - n_{IY}$ section. If, on the other hand we rotate from a definite polarization state of qubit 1 to a definite polarization state of qubit 2, we find a square cross-section; examples are the $n_{IX} - n_{XI}$ or $n_{IX} - n_{YI}$ sections. Rotations of \vec{n} that mix single-qubit-type and correlation-type directions can be of either shape; the $n_{IX} - n_{XX}$ section is square, while

	1	2	3	4	5	6	7	8	9	10	11	12	13	14	15
IX	1														
IY	2	D													
IZ	3	D	D												
XI	4	S	S	S											
XX	5	S	D	D	S										
XY	6	D	S	D	S	D									
XZ	7	D	D	S	S	D	D								
YI	8	S	S	S	D	D	D	D							
YX	9	S	D	D	D	D	S	S	S						
YY	10	D	S	D	D	S	D	S	S	D					
YZ	11	D	D	S	D	S	S	D	S	D	D				
ZI	12	S	S	S	D	D	D	D	D	D	D	D			
ZX	13	S	D	D	D	D	S	S	D	D	S	S	S		
ZY	14	D	S	D	D	S	D	S	D	S	D	S	S	D	
ZZ	15	D	D	S	D	S	S	D	D	S	S	S	S	D	D

TABLE I. Two dimensional sections of the full two-qubit state space M , keeping only two components of the polarization vector non-zero. Type S is the square section, while type D is the disc section. The table is symmetric thus the upper part is omitted. The diagonal entries do not correspond to two dimensional sections.

the $n_{IX} - n_{YY}$ section is a disc. Finally, rotations between correlation-type directions can have either shape. The $n_{XX} - n_{XY}$ section corresponds to a local rotation of qubit 2; hence it is a disc. Rotations involving both qubits, such as that which generates the $n_{XX} - n_{YY}$ section, generally give square sections.

We may conclude that M is a highly dimpled ball, perhaps most similar in shape to a golf ball. Its minimum radius is $|\vec{n}| = 1$ and its maximum radius is $|\vec{n}| = \sqrt{3}$.

Since our aim is to quantify entanglement in M , we need an entanglement measure. We will employ C , the concurrence of Wootters [3]. The concurrence varies from 0 for separable states to 1 for maximally entangled state, i.e., the Bell-like states. It is defined as $C = \max\{0, q\}$, and

$$q = \lambda_1 - \lambda_2 - \lambda_3 - \lambda_4,$$

where λ_i are the square roots of the eigenvalues of the matrix $\rho_{AB}\tilde{\rho}_{AB}$ arranged in decreasing order and

$$\tilde{\rho}_{AB} = (\sigma_y^A \otimes \sigma_y^B) \rho_{AB}^* (\sigma_y^A \otimes \sigma_y^B), \quad (9)$$

is a spin-flipped density matrix. ρ_{AB}^* is the complex conjugate of the density matrix ρ_{AB} . It is not possible to write the function $C(\vec{n})$ in a simple explicit form unless further restrictions on \vec{n} apply [38], but it is clear from the form of the continuous function $q(\vec{n})$ and the presence of the max function that C is a continuous but not an analytic function of \vec{n} .

We next consider S , the manifold of separable states, which we define as those \vec{n} for which the concurrence vanishes: $C(\vec{n}) = 0$. S is a subset of M and $M \setminus S$ is the set of entangled states. S includes the origin since $q(\vec{0}) = -1/2$ and $C(\vec{0}) = \max\{0, q(\vec{0})\} = 0$. Since $q(\vec{n})$ is continuous, S actually includes a ball of finite radius

about the origin: it can be shown that if $|\vec{n}| \leq 1/\sqrt{3}$, then $\vec{n} \in S$ [39]. Thus the manifold of separable states has finite volume in M : S is also 15-dimensional. We will also refer below to the interiors and boundaries of M and S and denote these by $\text{Int}(M)$, B_M , $\text{Int}(S)$, and B_S . Since the various sets we encounter in this paper are not linear subspaces, we need the general topological definitions of “boundary”, “interior” and “dimension”. These may be found, for example, in Ref. [40].

S is also a convex set. What else can we say about the shape of S ? It is easily seen that the surface of S , like that of M , is rather non-spherical. Indeed $C = 0$ along any of the basis vector directions. Coupled with the fact that S is convex, we see that S must contain a large hyperpolygon with vertices at $\vec{n} = (\pm 1, 0, 0, \dots, 0)$, $\vec{n} = (0, \pm 1, 0, 0, \dots, 0)$, etc. $C(\vec{n})$ is invariant under local rotations, so it has the same hyper-cylindrical symmetry as M . Again we may consider 2-dimensional sections in order to understand the shape of the surface. Two examples are shown in Fig. 1.

A simple-sampling Monte Carlo study shows that there are more entangled states than separable states in M . The details can be found in Appendix B.

III. DYNAMICAL EVOLUTION IN S

A. introduction

The dynamical evolution or trajectory of a quantum system is a function $\vec{n}(t)$ with $t \in [0, \infty)$ and $\vec{n} \in M$. The initial point is $\vec{n}(0)$ and, in the cases of interest here, the trajectory approaches a limiting point as $t \rightarrow \infty$ and we can define $\vec{n}_\infty = \lim_{t \rightarrow \infty} \vec{n}(t)$. The entanglement evolution is the associated function $C(t) = C(\vec{n}(t))$. $C \in [0, 1]$. For studies of decoherence the main interest is in entanglement evolutions such that $C(0) > 0$ and $C(\infty) = 0$, i.e., the system starts in an entangled state and ends in a separable state. Four distinct categories of entanglement evolution of this type have been seen in model studies [42]. They are shown in Fig. 2. These four categories are topologically distinct, as may be seen by considering the set $T_0 \equiv \{t | C(t) = 0\}$. In category \mathcal{A} , T_0 is the null set; in category \mathcal{E} , T_0 is a single infinite interval; in category \mathcal{B} , T_0 is a set of discrete points; in category \mathcal{O} , T_0 is a union of disjoint intervals.

These categories also reflect how the trajectory traverses S and $M \setminus S$. Entanglement evolutions in category \mathcal{A} approach the boundary of separable and entangled regions asymptotically from the entangled side. The trajectories never hit S while the decrease in entanglement may or may not be monotonic, as seen in Ref. [43]. Entanglement evolutions in category \mathcal{B} bounce off the surface of S at finite times but never enter S . Overall, entanglement diminishes nonmonotonically. Entanglement evolutions in category \mathcal{E} enter S at finite time and entanglement stays zero afterwards. This is the typical ESD behavior. Entanglement evolutions in category \mathcal{O} give ESB: after

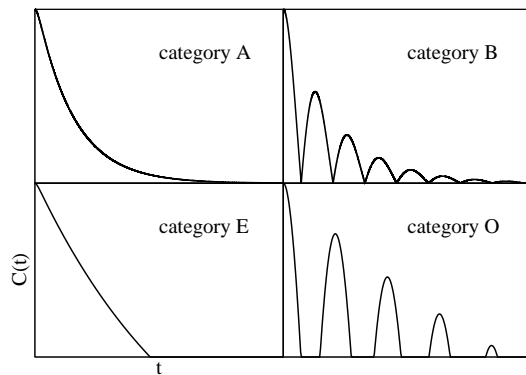


FIG. 2. Four categories of entanglement evolution. \mathcal{A} : approaching. \mathcal{B} : bouncing. \mathcal{E} : entering. \mathcal{O} : oscillating.

ESD, entanglement suddenly appears after some dark period.

We shall focus on models with associated linear maps Λ , i.e., $\rho(t) = \Lambda(t)[\rho(0)]$. More general non-linear models may be contemplated, but they seem to have unphysical features [44]. It is known that $\Lambda(t)$ is completely positive (CP) if and only if there exists a set of operators $\{E_a\}$ such that [2]

$$\Lambda[\rho(0)] = \sum_a E_a \rho(0) E_a^\dagger. \quad (10)$$

We require Λ to be trace preserving so that it maps density matrix to density matrix. This condition is equivalent to the completeness condition $\sum_a E_a E_a^\dagger = I$. In terms of the polarization vector, the dynamics is described by an affine map $\Upsilon(t)$ acting on the initial polarization vector $\vec{n}(0)$, i.e.

$$\begin{aligned} \vec{n}(t) &\equiv \Upsilon(t) [\vec{n}(0)] \\ &= T(t) \vec{n}(0) + \vec{m}(t) \end{aligned} \quad (11)$$

where $T(t)$ is a real matrix and $\vec{m}(t)$ is a real vector [33]. $\vec{m}(t)$ is zero for all time only when $\Upsilon(t)$ is unital, i.e., it maps $\vec{0}$ to $\vec{0}$ (in terms of Λ , the unital property means that Λ maps identity matrix to identity matrix). $T(0) = I$ and $\vec{m}(0) = \vec{0}$.

Coherent dynamics is described by unitary transformations on the density matrix (single Kraus operator). The dynamical map $\Upsilon(t)$ is then linear which translates to orthogonal transformations T acting on the polarization vector \vec{n} . Decoherent dynamics (multiple Kraus operators) is characterized by the nonorthogonality of the transfer matrix T . Markovian dynamics is conventionally defined by Υ possessing the semigroup property $\Upsilon(t_1 + t_2) = \Upsilon(t_2)\Upsilon(t_1)$, which translates to

$$T(t_1 + t_2) = T(t_2)T(t_1) \quad (12)$$

$$\vec{m}(t_1 + t_2) = T(t_2)\vec{m}(t_1) + \vec{m}(t_2). \quad (13)$$

We shall adopt a slightly different definition of Markovianity for the present paper. An evolution will be said

to be “distance Markovian” if $|\vec{n}(t) - \vec{n}_\infty|$ is a monotonically decreasing function. Note “distance Markovian” is a weaker condition than Markovian, though the two are usually equivalent. Given the semigroup property Eq. 12 and Eq. 13, we have

$$\begin{aligned} |\vec{n}(t) - \vec{n}_\infty| &= |[T(t)\vec{n}(0) + \vec{m}(t)] - [T(t)\vec{n}_\infty + \vec{m}(t)]| \\ &\leq \|T(t)\| |\vec{n}(0) - \vec{n}_\infty| \\ &\leq |\vec{n}(0) - \vec{n}_\infty| \end{aligned}$$

since all eigenvalues of $T(t)$ have their norms in the range 0 to 1, i.e., $T(t)$ cannot increase the purity of the quantum state.

Any model of an open quantum system defines a set of possible dynamical evolutions. This is done by specifying the equations of motion, which give T , \vec{m} and the initial conditions, which give $\vec{n}(0)$. We define the dynamical subspace D of a model as the set of all trajectories allowed by the set of initial conditions and the equations of motions. Eq. 11 shows that, as long as the set of all initial conditions is a linear space (the usual case), then D is a linear space intersected with M : we first choose a basis that spans the set of all possible $\vec{n}(0)$, then evolve this basis according to Eq. 11, giving a linear subspace in the space of all \vec{n} . A precise and general definition of D is given in Appendix C. The set of *admissible* \vec{n} is then given by intersecting this linear subspace with M . D is a manifold of any dimension from 1 to 15 in the two-qubit case. We note $\dim D$ could be smaller than $\dim M$. This happens when both $\rho(0)$ and $E_a(t)$ are expandable by identity and a true subalgebra \mathfrak{a} of $su(N)$. $\dim D$ is then equal to the number of independent elements in \mathfrak{a} . For example, if $\rho(0)$ is a two-qubit “X-state” and the dynamics can be described by the action of Kraus operators in the X-form, the dynamical subspace D will be 7-dimensional [45].

It is the nature of the intersection of D with S and the position of \vec{n}_∞ relative to S that determines the categories of entanglement evolution of a model.

The aim of the remainder of this paper is to show how to determine the topological structure of $D \cap S$ and the position \vec{n}_∞ for various illustrative models of increasing complexity, and then to deduce the possible entanglement evolutions from this information. We note that in general D can be determined without fully solving the dynamics. Thus it is possible to gain qualitative information of the entanglement evolution of the model with simple checks.

B. Model D_3

Our first model consists of two qubits (A and B) with a Heisenberg interaction and classical dephasing noise on one of the qubits. The Hamiltonian is

$$H(t) = -\frac{1}{2} [J\vec{\sigma}^A \cdot \vec{\sigma}^B + s(t)g\sigma_z^B + B_0\sigma_z^A], \quad (14)$$

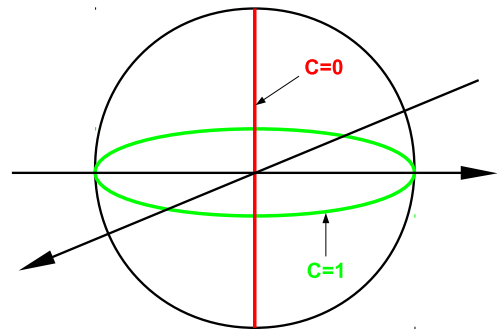


FIG. 3. (Color online) Effective Bloch sphere representation for the dynamical subspace D_3 . The north and south pole are either $\{|10\rangle, |01\rangle\}$ or $\{|00\rangle, |11\rangle\}$. States resting on the red line connecting north and south pole have zero concurrence. States on the green equator are equivalent to Bell states thus maximally entangled.

where $s(t)$ is a random function. This is a classical noise model. To compute $\vec{n}(t)$ we need to average over a probability functional for $s(t)$, which we will specify more precisely below. Note that the manifold spanned by $\{|00\rangle, |11\rangle\}$ is decoupled from the manifold spanned by $\{|01\rangle, |10\rangle\}$ under the influence of this Hamiltonian. Thus if the initial density matrix lies in one of the two subspaces, the four-level problem decouples into two two-level problems and we can use the Bloch ball representation to visualize the state space and entanglement evolution.

Take the initial state to be in $\text{span}\{|00\rangle, |11\rangle\}$ for example. The dynamical subspace D_3 is a 3-dimensional ball, as shown in Fig. 3. This makes it relatively easy to visualize the state and entanglement evolution. However, note that the center of D_3 is *not* the state $\vec{n} = \vec{0}$. In fact, all the points on the z -axis belong to B_S because every neighborhood of any of these points contains points for which $C > 0$.

The square roots of the non-zero eigenvalues of $\rho\tilde{\rho}$ are $\lambda_{1,2} = (\sqrt{1 - r^2 \cos^2 \theta} \pm r \sin \theta)/2$, where r and θ are the spherical coordinates of the ball, and $\tilde{\rho}$ is the spin-flipped density matrix, as in Eq. 9. The concurrence is given by

$$C = r \sin \theta. \quad (15)$$

The maximally entangled states are on the equator and the separable states are on the z -axis, as seen in Fig. 3. The concurrence has azimuthal symmetry and is linear in the radial distance from the z -axis. The separable states in D_3 form the 1-dimensional line $D_3 \cap S$ that connects the north and south poles of D_3 .

The key point is that $D_3 \cap S$ has a lower dimension than D_3 itself. Now consider the possible trajectories with \vec{n}_∞ on the z -axis. No function $\vec{n}(t)$ with continuous first derivative can have a finite time interval with $C(t) = 0$. The trajectories either hit the z -axis at discrete time instants which puts them in category \mathcal{B} , or approach the z -axis asymptotically which puts them in category \mathcal{A} .

Let us specify $s(t)$ in more detail to demonstrate how those two qualitatively different behaviors are related to Markovianity. Qubit A sees a static field B_0 while qubit B sees a fluctuating field $s(t)g$. All fields are in the z -direction. We will take the noise to be random telegraph noise (RTN): $s(t)$ assumes value ± 1 and switches between these two values at an average rate γ . RTN is widely observed in solid state systems [46–49].

For this dephasing noise model, the above-mentioned decoupling into two 2-dimensional subspaces occurs. In the 2×2 block labelled by $\{|00\rangle, |11\rangle\}$ we find

$$H(t) = -\frac{\sigma_z}{2} [s(t)g + B_0],$$

where σ_z is the Pauli matrix in the subspace.

This Hamiltonian can be solved *exactly* using a quasi-Hamiltonian method [32]. The time-dependent decoherence problem can be mapped exactly to a time-independent problem where the two-value fluctuating field is described by a spin half particle. The quasi-Hamiltonian is given by

$$H_q = -i\gamma + i\gamma\tau_1 + L_z(B_0 + \tau_3g),$$

where τ_i are the Pauli matrices of the noise ‘‘particle’’. L_z is the $SO(3)$ generator in the $\{|00\rangle, |11\rangle\}$ space.

The transfer matrix is given by

$$T(t) = \begin{bmatrix} \zeta_T(t) \cos B_0 t & \zeta_T(t) \sin B_0 t & 0 \\ -\zeta_T(t) \sin B_0 t & \zeta_T(t) \cos B_0 t & 0 \\ 0 & 0 & 1 \end{bmatrix} \quad (16)$$

where

$$\zeta_T(t) = e^{-\gamma t} \left[\cos(\Omega t) + \frac{\gamma}{\Omega} \sin(\Omega t) \right] \quad (17)$$

$$\Omega = \sqrt{g^2 - \gamma^2} \quad (18)$$

is the dephasing function due to RTN and it describes the phase coherence in the x - y plane [19]. $\vec{n}(t) = 0$ since the dynamics is unital. Note $\zeta_T(t)$ has qualitatively different behaviors in the $g \leq \gamma$ and $g > \gamma$ regions, as the trigonometric functions become hyperbolic functions [32].

Taking $|\Phi+\rangle = (|00\rangle + |11\rangle)/\sqrt{2}$ as initial state, the effective Bloch vector is

$$\vec{n}(t) = \begin{bmatrix} \zeta_T(t) \cos B_0 t \\ -\zeta_T(t) \sin B_0 t \\ 0 \end{bmatrix}. \quad (19)$$

The state trajectory is fully in the equatorial plane, as seen in Fig. 4. The dephasing function $\zeta_T(t)$ modulates

the radial variation and the static field B_0 provides precession.

$$|\vec{n}(t) - \vec{n}_\infty| = |\zeta_T(t)|, \quad (20)$$

and the dynamics is distance Markovian if $g \leq \gamma$ ($\zeta_T(t)$ being monotonic). In this parameter region, $\zeta_T(t)$ can be approximated by $\exp(-g^2/2\gamma)$ and the dynamics is approximately Markovian as well. Thus we do not need to distinguish Markovian and distance Markovian in this model. In the Markovian case, the monotonicity of ζ_T gives rise to spiral while in the non-Markovian case the state trajectory periodically spirals outwards with frequency Ω . In both cases, the limiting state is the origin of the ball.

The concurrence evolution is given by

$$C(t) = |\zeta_T(t)|.$$

Thus Markovian noise gives rise to entanglement evolutions in category \mathcal{A} while non-Markovian noise gives rise to that in category \mathcal{B} . Entanglement evolutions in the other two categories can not occur due to fact that $\dim(D_3 \cap S) < \dim(D_3)$.

C. Model D_8

In the previous section we saw that dynamical subspaces spanned by two computational basis states does not possess the property $\dim D \cap S = \dim D$. A natural question is whether simply increasing the number of basis states helps. This can be done by choosing a Hamiltonian that connects only the triplet states in the original Hilbert space. One example would be

$$H = J(t) \vec{\sigma}^A \cdot \vec{\sigma}^B,$$

as in Ref. [50], where the Heisenberg coupling $J(t)$ has time dependence and is modeled as a classical random process.

Note this Hamiltonian conserves the total angular momentum of the two qubits. As a result, the triplet space spanned by $\{|00\rangle, |11\rangle, (|10\rangle + |01\rangle)/\sqrt{2}\}$ is decoupled from the singlet space. Thus the dynamical subspace D has its basis elements in $su(3)$ if we choose the initial state to be in the triplet subspace.

Using Gell-Mann matrices as the elements of $su(3)$ algebra, the state space is a subset of a ball in \mathbb{R}^8 [29].

$$\rho = \frac{1}{2}I + \frac{1}{2} \sum_{i=1}^8 m_i \mu_i$$

and μ_i satisfies

$$\mu_i = \mu_i^\dagger, \quad \text{Tr } \mu_i = 0, \quad \text{Tr } \mu_i \mu_j = 2\delta_{ij}.$$

The m_i are linearly related to the previously defined n_i . The square roots of the eigenvalues of $\rho \bar{\rho}$ are

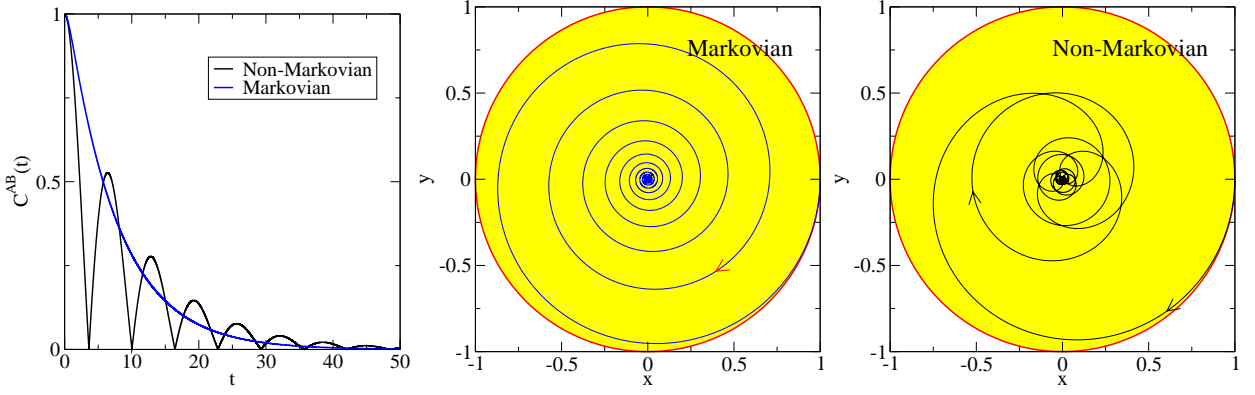


FIG. 4. (Color online) (a) Entanglement evolution and (b), (c) state trajectories in the dynamical subspace D_3 with RTN for Markovian and Non-Markovian evolutions. Concurrence is equal to the absolute value of $\zeta_T(t)$. State trajectory in the equatorial plane of the effective Bloch representation where the only separable state is the origin $\vec{0}$. The initial state is the Bell state $|\Phi^+\rangle$. The concurrence is given by the radial distance. In both cases, $g = 0.5$, $B_0 = 1$. $\gamma = 1$ for the Markovian case and $\gamma = 0.1$ for the Non-Markovian case.

$$\lambda_{1,2} = \left| \frac{1}{2} \sqrt{m_6^2 + m_7^2} \pm \frac{\sqrt{2}}{6} \sqrt{2 - \sqrt{3} (\sqrt{3}m_3 + m_8) + 3m_8 (\sqrt{3}m_3 - m_8)} \right|, \quad \lambda_{3,4} = 0 \quad (21)$$

Thus the set $D_8 \cap S$ of separable states is composed of two geometric objects: $m_6 = m_7 = 0$ which is in \mathbb{R}^6 and

$$2 - \sqrt{3} (\sqrt{3}m_3 + m_8) + 3m_8 (\sqrt{3}m_3 - m_8) = 0$$

which is in \mathbb{R}^7 . In addition to a concurrence-zero hyperline, we have a $C = 0$ hyperplane in D_8 . Hence $\dim(D_8 \cap S) < \dim(D_8)$ and this model only displays entanglement evolutions in categories \mathcal{A} and \mathcal{B} .

Introducing extra dimensions thus helps to form non-zero volume of $D \cap S$ in D but a Hilbert space spanned by three of the four computational basis states is still not enough. D_3 and D_8 both avoid the region near the fully mixed state $\vec{0}$, where most separable states reside [51]. This region is included in the dynamical subspaces in the next two sections.

Note that for D_3 and D_8 , the symmetry of the Hamiltonian and the specification of the initial conditions allow us to fully describe the dynamical subspace without explicitly solving the dynamics. This feature can be seen in the more complicated models in the following sections as well: entanglement evolution categories, as a qualitative property of the system dynamics, can be determined from symmetry considerations of the model (dynamics plus initial condition), position of \vec{n}_∞ in $D \cap S$ and the memory effect of the environment.

D. Model YE

Yu and Eberly considered a disentanglement process due to spontaneous emission for two two-level atoms in two cavities. In this case the decoherence clearly acts independently on the two qubits. Nevertheless they found that ESD occurs for specific choices of initially entangled states [7].

The decoherence process is formulated using the Kraus operators

$$\rho(t) = \sum_{\mu=1}^4 K_\mu(t) \rho(0) K_\mu^\dagger(t), \quad (22)$$

where $K_\mu(t)$ satisfy $\sum_{\mu} K_\mu^\dagger K_\mu = I$ for all t [2, 52]. For the atom-in-cavity model, they are explicitly given by

$$K_1 = F_1 \otimes F_1, \quad K_2 = F_1 \otimes F_2 \quad (23)$$

$$K_3 = F_2 \otimes F_1, \quad K_4 = F_2 \otimes F_2, \quad (24)$$

where

$$F_1 = \begin{bmatrix} \gamma & 0 \\ 0 & 1 \end{bmatrix}, F_2 = \begin{bmatrix} 0 & 0 \\ \omega & 0 \end{bmatrix}, \quad (25)$$

and $\gamma = \exp(-\Gamma t/2)$ and $\omega = \sqrt{1 - \exp(-\Gamma t)}$.

It is possible to choose initial states such that the density matrices have the following form for all t

$$\rho(t) = \frac{1}{3} \begin{bmatrix} a(t) & 0 & 0 & 0 \\ 0 & b(t) & z(t) & 0 \\ 0 & z(t) & c(t) & 0 \\ 0 & 0 & 0 & d(t) \end{bmatrix} \quad (26)$$

with

$$a(t) = \kappa^2 a_0, \quad (27)$$

$$b(t) = c(t) = \kappa + \kappa(1 - \kappa)a_0, \quad (28)$$

$$d(t) = 1 - a_0 + 2(1 - \kappa) + (1 - \kappa)^2 a_0, \quad (29)$$

$$z(t) = \kappa. \quad (30)$$

where $\kappa = \exp(-\Gamma t)$. Here the parameter a_0 determines the initial condition.

The two-qubit entanglement is

$$C(t) = \frac{2}{3} \max\{0, \kappa f(t)\}, \quad (31)$$

where $f(t) = 1 - \sqrt{a_0[1 - a_0 + 2(1 - \kappa) + (1 - \kappa)^2 a_0]}$.

In the polarization vector representation, the dynamics defined by Eq. 22 can be given explicitly by the transfer matrix $T(t)$ and the translation vector $\vec{m}(t)$

$$T(t) = \begin{pmatrix} \kappa & 0 & 0 & 0 & 0 \\ 0 & \kappa & 0 & 0 & 0 \\ 0 & 0 & \kappa & 0 & 0 \\ 0 & 0 & 0 & \kappa & 0 \\ \kappa^2 - \kappa & 0 & 0 & \kappa^2 - \kappa & \kappa^2 \end{pmatrix}, \quad (32)$$

and

$$\vec{m}(t) = [\kappa - 1; 0; 0; \kappa - 1; (\kappa - 1)^2]. \quad (33)$$

Here the coordinates are $\{n_{IZ}, n_{XX}, n_{YY}, n_{ZI}, n_{ZZ}\}$. We note that Eqs. 12 and 13 are satisfied and this spontaneous emission model is Markovian and distance Markovian.

The non-zero components are

$$n_{IZ}(t) = n_{ZI}(t) = -1 + \frac{2}{3}(1 + a_0)\kappa \quad (34)$$

$$n_{XX}(t) = n_{YY}(t) = \frac{2}{3}\kappa \quad (35)$$

$$n_{ZZ}(t) = 1 - \frac{4}{3}(1 + a_0)\kappa + \frac{4}{3}a_0\kappa^2. \quad (36)$$

and the limiting state is

$$\vec{n}_\infty = (-1, 0, 1), \quad (37)$$

where the coordinates are (n_{IZ}, n_{XX}, n_{ZZ}) .

This shows that the dynamical subspace D_Y is a 3-dimensional section of M where the non-zero components are $n_{IZ}, n_{ZI}, n_{XX}, n_{YY}$, and n_{ZZ} but also $n_{IZ} = n_{ZI}$ and $n_{XX} = n_{YY}$, such that it can also be visualized in three dimensions. Interestingly, the limiting state \vec{n}_∞ due to spontaneous emission is on the boundary of set S of separable states, and the purity of the state increases with time.

Although we have so far fully solved the system dynamics, for the purpose of describing D_Y , it is enough to know that $\{IZ, ZI, XX, YY, ZZ\}$ are the basis of D_Y and that the Kraus operators preserve the equalities $n_{IZ} = n_{ZI}$, $n_{XX} = n_{YY}$ from the initial conditions. D_Y is then

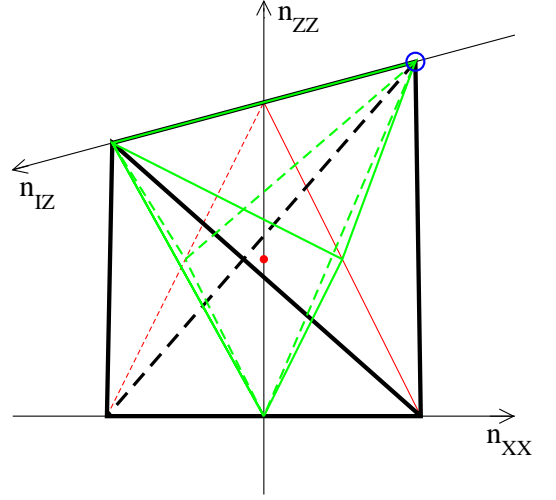


FIG. 5. (Color online) The dynamical subspace D_Y is a tetrahedron outlined by black lines. The set of separable states $D_Y \cap S$ form a hexahedron outlined by green lines. The origin (fully mixed state $\vec{n} = \vec{0}$) is denoted by a red filled dot. The limiting state \vec{n}_∞ in Ref. [7] is denoted by a blue circle.

determined from the positivity condition of the density matrix.

The positivity condition for the density matrix is given by

$$a_2 \geq 0 \Rightarrow 2n_{IZ}^2 + 2n_{XX}^2 + n_{ZZ}^2 \leq 3$$

$$a_3 \geq 0 \Rightarrow 2n_{IZ}^2 + 2n_{XX}^2 + n_{ZZ}^2 \leq 1 + 2n_{ZZ}(n_{IZ}^2 - n_{XX}^2)$$

$$a_4 \geq 0 \Rightarrow AB \geq 0$$

where $A = (1 + n_{ZZ})^2 - 4n_{IZ}^2$ and $B = (1 - n_{ZZ})^2 - 4n_{XX}^2$. At $t = 0$, $\vec{n}_0 = (2a_0 - 1, 2, -1)/3$. The positivity constraint $a_3 \geq 0$ gives rise to the range of the possible initial conditions, parametrized by $a_0 \in [0, 1]$.

The square roots of the eigenvalues of $\rho\bar{\rho}$ are

$$\lambda_a = \lambda_b = \frac{1}{4}\sqrt{A} \quad (38)$$

$$\lambda_c = \frac{1}{4}|1 - n_{ZZ} + 2n_{XX}| \quad (39)$$

$$\lambda_d = \frac{1}{4}|1 - n_{ZZ} - 2n_{XX}| \quad (40)$$

The ordering of the λ 's can change during the course of an evolution. When λ_a is the largest one finds $C = 0$, which is helpful in determining B_S .

D_Y is a tetrahedron with vertices at $(0, -1, -1)$, $(0, 1, -1)$, $(-1, 0, 1)$, and $(1, 0, 1)$, as seen in Fig. 5. $D_Y \cap S$ is a hexahedron that shares some external areas with D_Y . The 2-dimensional section of D_Y with $n_{IZ} = 0$ is shown in Fig. 6. On the other hand, if the section is done with $n_{XX} = 0$, we get a upside down triangle made of separable states, as shown in Fig. 7.

Yu and Eberly showed that a sudden transition of the entanglement evolution from category \mathcal{A} to category \mathcal{E} is possible as one tunes the physical parameter a_0 . This

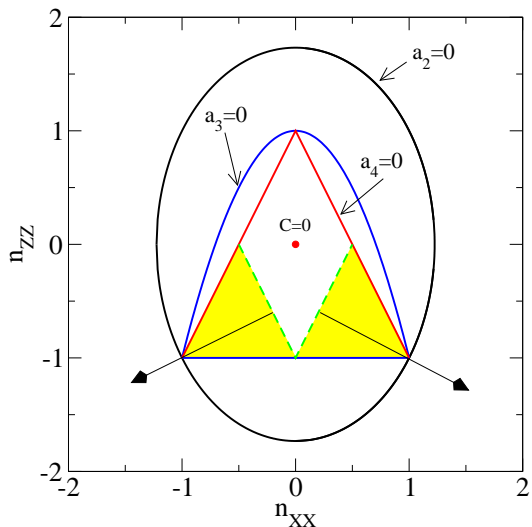


FIG. 6. (Color online) Cross section of the dynamical subspace D_Y with $n_{IZ} = 0$ and D_Z with $n_{XY} = 0$. $a_2 = 0$ is the ellipse. $a_3 = 0$ gives the parabola and the bottom of the isosceles triangle. $a_4 = 0$ sets the two sides of the triangle. The entangled region is shaded where the filled arrows denote increasing direction of the concurrence. The green dashed line is the boundary of entangled and separable states. The fully mixed state is denoted by a red dot.

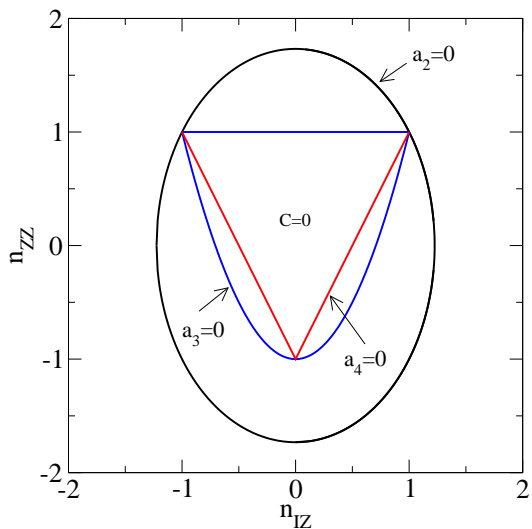


FIG. 7. (Color online) Cross section of the dynamical subspace D_Y with $n_{XX} = 0$. $a_2 = 0$ is the ellipse. $a_3 = 0$ gives the parabola and the top of the isosceles triangle. $a_4 = 0$ sets the two sides of the triangle. The whole section is filled with separable states.

phenomenon can be easily understood in our formalism, as seen in Fig. 8. The curvature of the state trajectories vary as the initial state changes. Thus there is a continuous range of initial states parametrized by a_0 whose trajectories enter $S \cap D_Y$ within finite amount of time and also a continuous range of initial states whose trajectories never enter $\text{Int}(S)$. Note Fig. 8 is a schematic

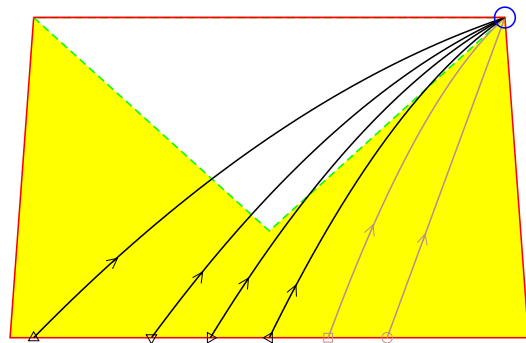


FIG. 8. (Color online) Schematic drawing of the different types of entanglement evolutions in the dynamical subspace D_Y . The limiting state \vec{n}_∞ is denoted by a blue circle on the top right corner. Entanglement evolutions in category \mathcal{A} are brown-colored while those in category \mathcal{E} are black-colored.

drawing since the true state trajectories are truly three dimensional.

To be more quantitative, the transition between the category \mathcal{A} and category \mathcal{E} behaviors in the YE model could be determined by examining the angle θ_∞ between B_S and the tangent vector of the state trajectory in the long time limit. We denote the limiting tangent vector by $\vec{n}_T(\infty)$ and it is given by

$$\vec{n}_T(\infty) = (1 + a_0, 1, 4a_0 - 2). \quad (41)$$

The relevant B_S in the YE model is a plane passing defined by the following three points: \vec{n}_∞ , $(0, 0, -1)$ and $(0, 1/2, 0)$. It is parametrized by

$$\hat{m} \cdot (\vec{n} - \vec{n}_\infty) = 0, \quad (42)$$

where $\hat{m} = (2, -2, 1)/3$ is the unit normal of the plane pointing into the separable region $S \cap D_Y$. Note $\vec{m} \cdot \vec{n}_T(\infty) = (6a_0 - 2)/3$ is proportional to $\cos \theta_\infty$ and its sign tells us whether the state trajectory approaches \vec{n}_∞ from the separable region or the entangled region. Since $0 \leq a_0 \leq 1$, $\vec{m} \cdot \vec{n}_T(\infty)$ falls in the range $[-2/3, 4/3]$ and both the ESD and HL behaviors are possible.

The condition

$$\vec{m} \cdot \vec{n}_T(\infty) = 0, \quad (43)$$

i.e., $a_0 = 1/3$, gives rise to the critical trajectory which approaches \vec{n}_∞ along B_S . When $\vec{m} \cdot \vec{n}_T(\infty) > 0$, i.e., $a_0 \in [1/3, 1]$, the state trajectory approaches \vec{n}_∞ from the entangled region and we get entanglement evolutions in category \mathcal{A} . These trajectories are represented by the brown curves in Fig. 8. On the other hand, when $\vec{m} \cdot \vec{n}_T(\infty) \leq 0$, i.e., $a_0 \in [0, 1/3)$, the state trajectory approaches \vec{n}_∞ from the separable region and we get entanglement evolutions in category \mathcal{E} . These trajectories are represented by the black curves in Fig. 8.

The key point about the model YE is that the limiting state $\vec{n}_\infty \in B_S$: it is on the boundary of the entangled and separable regions. That is why entanglement evolutions in both category \mathcal{A} and category \mathcal{E} are possible.

E. Model ZJ

Here we present a physically motivated dynamical subspace where the dynamics satisfies the following conditions: 1) the two qubits are not interacting; 2) the noises on the qubits are not correlated; 3) the effect of dephasing and relaxation can be separated. This model shows all four categories of entanglement evolution.

For this model the two-qubit dynamics can be decomposed into single-qubit dynamics [19]. The extended two-qubit transfer matrix is $\underline{T}(t) = \underline{R}^A \otimes \underline{R}^B$ where

$$\underline{R}(t) = \begin{bmatrix} 1 & 0 & 0 & 0 \\ 0 & \zeta(t) \cos B_0 t & \zeta(t) \sin B_0 t & 0 \\ 0 & -\zeta(t) \sin B_0 t & \zeta(t) \cos B_0 t & 0 \\ 0 & 0 & 0 & e^{-\Gamma_1 t} \end{bmatrix}$$

is the extended transfer matrix of individual qubits. The top left entry 1 describes the dynamics of I and is there only for notational convenience. Here $\zeta(t)$ describes dephasing process, Γ_1 is the longitudinal relaxation rate and B_0 is static field in the z direction that causes Larmor precession. $\zeta(0) = 1$ and $\zeta(\infty) = 0$ if dephasing occurs. Note this dynamical description of decoherence is completely general as long as one can separate dephasing and relaxation channels.

The dynamical subspace in this model is a specially parametrized 3-dimensional section of the full two-qubit state space M . Only the components n_{XX} , n_{XY} , n_{YX} , n_{YY} and n_{ZZ} are non-zero and we further have constraints $n_{XX} = n_{YY}$ and $n_{XY} = -n_{YX}$. We thus use $n_{XX,XY,ZZ}$ as independent parameters and the state space can be visualized in three dimensions. This dynamical subspace has been previously considered in Ref. [42] and we will call it D_Z .

The fact that $\dim D < \dim M$ relies on judicious choice of the initial states ρ_0 . In Ref. [19], more general initial states are considered such that D_Z is expanded into a dynamical subspace with 7 elements in the $su(4)$ algebra, i.e., $\{IX, XX, XY, YX, YY, ZI, ZZ\}$.

Note $n_{XX}^2 + n_{XY}^2 = R^2$ is conserved in D_Z . The positivity of the density matrix requires

$$a_2 \geq 0 \Rightarrow 2R^2 + n_{ZZ}^2 \leq 3 \quad (44)$$

$$a_3 \geq 0 \Rightarrow n_{ZZ} \leq 1 - 2R^2, \text{ and } n_{ZZ} \geq -1 \quad (45)$$

$$a_4 \geq 0 \Rightarrow 2R + n_{ZZ} \leq 1 \quad (46)$$

The concurrence is given by

$$C = \max \left\{ 0, R - \frac{1 + n_{ZZ}}{2} \right\}. \quad (47)$$

Separable states form a spindle shape on top and entangled states form a torus-like shape on bottom with triangular cross sections. A section along $n_{XY} = 0$ is shown in Fig. 6.

We have thus fully described the entanglement topology of D_Z and now we construct entanglement evolutions

that induce D_Z . A model similar to that of Eq. 14 that satisfies the three conditions is

$$H(t) = -\frac{1}{2} [s(t)\vec{g} \cdot \vec{\sigma}^B + B_0\sigma_z^A]. \quad (48)$$

Note the RTN has both dephasing (g_z) and relaxation (g_x, g_y) effects in this case. Situations with $n_{XY} = 0$ at intermediate qubit working point (with the presence of both dephasing and relaxation noise) have been considered in Ref. [42]. Here we choose the initial state to be the generalized Werner state [41]

$$w_r^\Phi = r|\Phi\rangle\langle\Phi| + \frac{1-r}{4}I_4, \quad (49)$$

where

$$|\Phi\rangle = \frac{1}{\sqrt{2}}(|00\rangle + e^{i\phi}|11\rangle) \quad (50)$$

is a Bell state.

The state trajectory is then given by

$$n_{XX}(t) = r \cos(2B_0 t)\zeta(t), \quad (51)$$

$$n_{XY}(t) = -r \sin(2B_0 t)\zeta(t), \quad (52)$$

$$n_{ZZ}(t) = re^{-\Gamma_1 t}. \quad (53)$$

Similarly, if the Werner state derived from the Bell state

$$|\Psi\rangle = \frac{1}{\sqrt{2}}(|01\rangle + e^{i\phi}|10\rangle) \quad (54)$$

is used as initial state, the state trajectory is

$$n_{XX}(t) = r\zeta_T(t), \quad (55)$$

$$n_{ZZ}(t) = -re^{-\Gamma_1 t}. \quad (56)$$

In both cases, the evolution of the concurrence is

$$C(t) = \max\{0, r[|\zeta(t)| - \xi(t)]\}$$

where $\xi(t) = (1 - re^{-\Gamma_1 t})/2$. Thus dephasing (relaxation) drives the state horizontally (vertically) towards the origin. Note ESD occurs whenever $\xi(t \rightarrow \infty) \neq 0$ and the corresponding limiting state is $\vec{n}_\infty = \vec{0}$ [19]. In the case of pure dephasing, $\Gamma_1 = 0$ and the trajectory moves in the horizontal plane $n_{ZZ} = -r$. The limiting state is $\vec{n}_\infty = (0, 0, -r)$. The only case where ESD does not happen is the pure dephasing processes on the $n_{ZZ} = -1$ plane since $\vec{n}_\infty \in B_S$. This amounts to $\xi(t) = 0$ and there is no abrupt cut-off.

At the pure dephasing point, $|\vec{n}(t) - \vec{n}_\infty| = \sqrt{2}r|\zeta(t)|$ and the dynamics is distance-Markovian if $\zeta(t)$ is monotonic. Since the typical Markovian dynamics can be characterized by $\zeta(t)$ with exponential decay forms, we do not distinguish Markovian and distance-Markovian for this model. Entanglement evolutions in categories \mathcal{E} and \mathcal{O} are possible, depending on whether the RTN is Markovian or non-Markovian, as seen in Fig. 9.

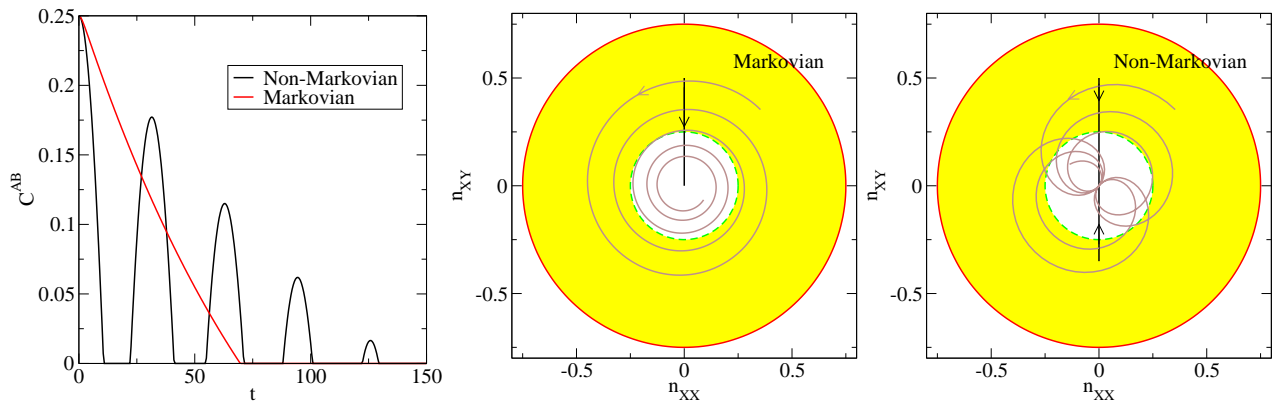


FIG. 9. (Color online) (a) Entanglement evolution and (b), (c) state trajectories in D_Z with pure dephasing noise. Only one qubit is subject to RTN and the other sees a static field B_0 . State trajectories with initial state $w_r^{\Psi+}$ is colored brown while those with initial state $w_r^{\Phi+}$ are colored black. $\zeta(t)$ is given by Eq. 17 and $\gamma = 0.5$, $g = 0.1$, $r = 0.5$, $B_0 = 0.1$.

If the initial state is on the $n_{ZZ} = -1$ plane, by tuning the relative weight of dephasing and relaxation noise, the entanglement evolution can transit from category \mathcal{A} to category \mathcal{E} if the noise is Markovian, or from category \mathcal{B} to category \mathcal{O} if the noise is non-Markovian [42]. These transitions can be interpreted as a transition of entanglement topology of the dynamical subspace as the physical parameter varies. At the pure dephasing point, D_Z shrinks to the $n_{ZZ} = -1$ disc and $\vec{n}_\infty \in B_S$. When this occurs we find \mathcal{A} and \mathcal{B} behavior.

IV. EVOLUTION CATEGORIES

Having given examples of models that produce the most important categories of entanglement evolution, we now provide a proof that the four categories essentially exhaust the possibilities. There are three cases.

Case 1. $\vec{n}_\infty \in \text{Int}(S)$, $\text{Image}(\vec{n})$ and B_S are transversal everywhere. Here $\vec{n} : [0, \infty) \rightarrow M$ is considered as a map from the time domain to the state space.

Consider a single trajectory $\vec{n}(t)$. The 1-dimensional manifold $\text{Image}(\vec{n}) \subset M$ and the 14-dimensional manifold B_S satisfy $\dim(M) = \dim[\text{Image}(\vec{n})] + \dim(B_S)$. Hence we can apply mod 2 intersection theory to the intersections of these two manifolds [53]. First assume that $\text{Image}(\vec{n})$ and (B_S) are transversal everywhere. (We discuss this assumption further below.) Since M is convex, we are guaranteed that there is a straight-line path from $\vec{n}(0)$ to \vec{n}_∞ and that the actual $\vec{n}(t)$ is homotopic to this path. The number of times that the straight-line path crosses B_S is one. The mod 2 intersection theorem then states that the number of times that $\vec{n}(t)$ crosses B_S is odd (formally, this is referred to as the cardinality of the 0-dimensional manifold $\vec{n}^{-1}(B_S)$). This yields two categories as we have defined them: $\text{card}\{\vec{n}^{-1}(B_S)\} = 1$ gives category \mathcal{E} , while $\text{card}\{\vec{n}^{-1}(B_S)\} = 3, 5, \dots$ gives category \mathcal{O} .

Case 2. $\vec{n}_\infty \in B_S$, $\text{Image}(\vec{n})$ and B_S are transversal

everywhere.

We are again assured of the existence of the straight-line path. However, this path can belong either to category \mathcal{A} : the path does not intersect B_S and the approach to \vec{n}_∞ is from $M \setminus S$, or to category \mathcal{E} : the path intersects B_S once, and the approach to \vec{n}_∞ is from S . Because S is convex, multiple intersections of the straight-line path with B_S are not allowed. All other paths are again homotopic to the straight-line path. The intersection theorem implies that if a general path approaches \vec{n}_∞ from $M \setminus S$, then it belongs to category \mathcal{A} or \mathcal{O} (in the variant where $C(t) > 0$ for $t > t_f$, for some finite t_f), while if the path approaches \vec{n}_∞ from S , then it belongs to category \mathcal{A} or \mathcal{O} (in the variant where $C(t) = 0$ for $t > t_f$).

Case 3. $\text{Image}(\vec{n})$ and B_S are not transversal everywhere.

There is the possibility that $\text{Image}(\vec{n})$ and B_S are not transversal at discrete values of t . This gives rise to quadratic or higher-order zeros of $C(t)$; the occurrence of such points is not of great interest since they lie in a set of measure zero that is not related to physical conditions. Of greater interest is the case when non-transversal points of intersection are due to restrictions placed on the paths that stem from physical restrictions placed on a model, e.g., a symmetry. For a given model we must then consider D , its dynamical subspace (a precise description of D is given in Appendix C). We must replace M by D , S by $D \cap S$, and B_S by $B_S \cap D$. The dimensions of these spaces are model-specific. For mod 2 intersection theory to apply, we need $\dim(D) = \dim[\text{Image}(\vec{n})] + \dim(B_S \cap D) = 1 + [\dim(S \cap D) - 1] = \dim(S \cap D)$. If this holds, then the reasoning applied to cases 1 and 2 can be repeated. However, it is also possible to have $\dim(S \cap D) < \dim(D)$ - we have seen an example in Fig. 3. In this case the intersections of $\text{Image}(\vec{n})$ and $B_S \cap D$ are never transversal. A generic path $\vec{n}(t)$ must either approach or “pierce” the low-dimensional space. This gives rise to \mathcal{A} and \mathcal{B} behaviors, respectively.

	$\dim(D \cap S) = \dim D$	$\dim(D \cap S) < \dim D$
$\vec{n}_\infty \in \text{Int}(S)$	\mathcal{E} or \mathcal{O}	\mathcal{A} or \mathcal{B}
$\vec{n}_\infty \in B_S$	$\mathcal{A}, \mathcal{B}, \mathcal{E}$ or \mathcal{O}	\mathcal{A} or \mathcal{B}

TABLE II. The relationships between entanglement evolution categories and details of the dynamics, such as the position of the limiting state \vec{n}_∞ , etc.

V. RESULTS AND CONCLUSIONS

We now summarize the results exemplified in Sec. III and formalized in Sec. IV by outlining a protocol to determine entanglement dynamics of any physical model.

For any physical model, the possible entanglement evolution categories are determined by three factors: the limiting point \vec{n}_∞ , the dynamical subspace D , and the presence or absence of distance-Markovianity. Once these questions are resolved, the possible entanglement evolutions are given by Table II.

\vec{n}_∞ is the fixed point of the asymptotic dynamics. Since it is determined by the long-time limit of the dynamics, it is usually fairly easy to compute. It may be a function of the parameters of the model. The crucial question about \vec{n}_∞ is whether it belongs to $\text{Int}(S)$, the interior of S (Row 1 of Table II) or B_S , the boundary of S (Row 2 of Table II). D is the collection of all trajectories of the model. It depends on all parameters of the model, and on their range of variation. A prescription for computing D has been given in Sec. III A. The crucial questions about D are its dimensionality $\dim(D)$ and the dimensionality of $\dim(D \cap S)$. If $\dim(D) = \dim(D \cap S)$ then Column 1 of Table II applies. If $\dim(D) < \dim(D \cap S)$ then Column 2 of Table II applies. Finally, non-distance-Markovian evolution gives \mathcal{B} and \mathcal{O} , while distance-Markovian evolution typically gives \mathcal{E} and \mathcal{A} .

Once the possible behaviors are known, one would like also to be able to compute the critical points or surfaces where transitions from one to another occur.

The first type of transition occurs when \vec{n}_∞ does not move between B_S and $\text{Int}(S)$, i.e., we stay in one row of the table. One cannot move between columns within a given model since D , by definition, represents all possible states of a model. Thus we stay in one box of the table. $\mathcal{E} \longleftrightarrow \mathcal{O}$ and $\mathcal{A} \longleftrightarrow \mathcal{B}$ are the possible transitions and the critical points represent a change from distance-Markovianity to non-distance-Markovianity. Such transitions may be subtle and difficult to calculate, and an explicit equation for the critical surface cannot be given. A quite simple example where the calculation can be done analytically has been given in Sec. III B.

The second type of transition happens when \vec{n}_∞ moves between B_S and $\text{Int}(S)$ and $\dim(D) = \dim(D \cap S)$ (Column 1). There will be a specific point at which this occurs. This point is determined by examining the asymptotic dynamics of the model as a function of the parameters. If the parameters are collectively given by a set $\{g_i\}$,

then the equation for the critical surface is $\vec{n}_\infty(g_i) \in B_S$. The transitions are $\mathcal{E} \longleftrightarrow \mathcal{A}$ and $\mathcal{O} \longleftrightarrow \mathcal{B}$ for distance-Markovian and non-distance-Markovian evolution. An example has been given in Sec. III E and Ref. [42].

The third type of transition occurs in Column 1, Row 2 of the table. In this case \vec{n}_∞ does not change, but the direction of approach to \vec{n}_∞ changes as a function of the parameters. In this case the equation of the critical surface is $\vec{n}_T(\infty) \in \text{tang}(B_S)$, where $\vec{n}_T(\infty)$ is the limiting tangent vector of the state trajectory and $\text{tang}(B_S)$ is the tangent space of the boundary of S . The transitions are $\mathcal{E} \longleftrightarrow \mathcal{A}$ and $\mathcal{O} \longleftrightarrow \mathcal{B}$ for distance-Markovian and non-distance-Markovian evolution. An example has been given in Sec. III D.

“Tricritical” points can also occur when more than one critical condition is satisfied.

Appendix A: two dimensional sections

With our conventions for the two-qubit $su(4)$ algebra, the structure constants can be calculated from

$$f_{ijk} = \frac{1}{2i \times 4} \text{Tr} [\mu_i, \mu_j] \mu_k \quad (\text{A1})$$

$$d_{ijk} = \frac{1}{2 \times 4} \text{Tr} [\mu_i, \mu_j]_+ \mu_k, \quad (\text{A2})$$

Here we denote $[\cdot, \cdot]_+$ as the anti-commutation operation. Most of them are zero and the non-zero structure constants are

$$\begin{aligned} 1 &= d_{1,4,5} = d_{1,8,9} = d_{1,12,13} = d_{2,4,6} = d_{2,8,10} \\ &= d_{2,12,14} = d_{3,4,7} = d_{3,8,11} = d_{3,12,15} = -d_{5,10,15} \\ &= d_{5,11,14} = d_{6,9,15} = -d_{6,11,13} = -d_{7,9,14} = d_{7,10,13} \\ &= f_{1,2,3} = f_{1,6,7} = f_{1,10,11} = f_{1,14,15} = -f_{2,5,7} \\ &= -f_{2,9,11} = -f_{2,13,15} = f_{3,5,6} = f_{3,9,10} = f_{3,13,14} \\ &= f_{4,8,12} = f_{4,9,13} = f_{4,10,14} = f_{4,11,15} = f_{5,8,13} \\ &= f_{5,9,12} = f_{6,8,14} = f_{6,10,12} = f_{7,8,15} = f_{7,11,12}. \end{aligned}$$

Suppose the two non-zero components of a two-dimensional section assume numerical values x and y . It can be shown that

$$\text{Tr} \rho^2 = \frac{1}{4}(1 + R^2) \quad (\text{A3})$$

$$\text{Tr} \rho^3 = \frac{1}{16}(1 + 3R^2) \quad (\text{A4})$$

$$\text{Tr} \rho^4 = \frac{1}{64}[1 + 6R^2 + R^4 + n_i n_j n_\ell n_m d_{ijk} d_{klm}], \quad (\text{A5})$$

where $R^2 = x^2 + y^2$. Note the generators μ_i as defined in Eq. 3 are elements of the Pauli group thus they either commute or anti-commute. This is the origin of the two geometrically different 2-dimensional sections in M .

If the two μ_i 's anti-commute, the d_{ijk} related term vanishes and the positivity constraints is solely on a_3 ,

$$a_3 \geq 0 \implies R^2 \leq 1. \quad (\text{A6})$$

This is the disc section. On the other hand, if the two μ_i 's commute, the d_{ijk} related term gives $4x^2y^2$. The positivity constraint is on a_4

$$a_4 \geq 0 \implies R^4 - 2R^2 - 2x^2y^2 + 1 \geq 0. \quad (\text{A7})$$

This gives rise to the square section.

Appendix B: volume estimation

The sets M and S are spheroids of varying radius and the set of entangled states $M \setminus S$ is a spheroidal shell of varying thickness. To get some idea of the volumes of M , S and $M \setminus S$ and their radial profiles we have performed Monte Carlo simulations on the sphere of radius $\sqrt{3}$ in \mathbb{R}^{15} . The results are shown in Fig. 10, where we give the probabilities that a state \vec{n} is physical (positive density matrix) and that it is separable, as a function of $|\vec{n}|$, leading to a radial probability distribution function for the physical states and the separable states. The distributions fall off fairly abruptly, which allows us to identify a rough ‘‘effective’’ radius of about $\sqrt{3}/2$ for the physical states and about $0.45 \times \sqrt{3}$ for the separable states. Plotted in this way, the entangled states form a rather thin shell. This is not the only way to display the data, of course. If the volume densities were to be plotted instead, the function shown would be multiplied by $|\vec{n}|^{14}$, and the density of separable states would show a sharp peak.

To estimate the volume of separable and physical states inside the 15 dimensional ball with radius $\sqrt{3}$, we first perform simple sampling Monte Carlo to get the radial distribution function $p(r)$ at various r values. Here $r = |\vec{n}|$. 10^{11} sample points are generated at each $r_k = \sqrt{3} \times 0.02k$. The accuracy of each $p(r_k)$ is beyond five digits. Uniformly distributed random numbers on a 14 dimensional sphere is generated using the algorithms in Ref. [54].

Take $p(r)$ to be the radial distribution for the physical states for example. To get V_{phys} from $p(r)$, we perform numerical integration using Simpson's rule.

$$V_{\text{phys}} [p(r)] = \frac{\int_0^{\sqrt{3}} p(r) r^{14} dr}{\int_0^{\sqrt{3}} r^{14} dr} V_B \quad (\text{B1})$$

$$= 15 V_B \int_0^1 p(\tilde{r}) \tilde{r}^{14} d\tilde{r}. \quad (\text{B2})$$

where $\tilde{r} = r/\sqrt{3}$ is the normalized radius, i.e., $|\vec{n}|/\sqrt{3}$. V_B it the volume of a 15-dimensional ball with radius $\sqrt{3}$

$$V_B \equiv V(r = \sqrt{3}, s = 15) \quad (\text{B3})$$

$$= \frac{\pi^{s/2}}{\Gamma(s/2 + 1)} r^s \simeq 1444.905 \quad (\text{B4})$$

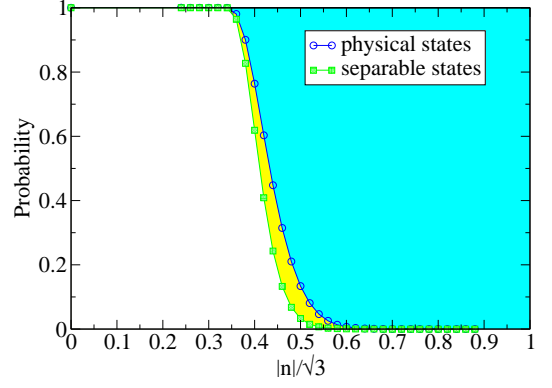


FIG. 10. Radial probability distribution functions of physical states (blue circle) and separable states (green square) in the ball of radius $\sqrt{3}$ in \mathbb{R}^{15} . For any fixed radius $|\vec{n}|$, the vertical span of the white, yellow and cyan regions denotes the probability of a randomly generated \vec{n} being separable, entangled and unphysical. The volume of S and M can be calculated from Eq. B2.

From the radial probability distributions of Fig. 10, we get the volume of separable states and physical states in the 15-dimensional polarization vector representation

$$V_{\text{sep}} = 0.008971 \pm 0.000005 \quad (\text{B5})$$

$$V_{\text{phys}} = 0.03700 \pm 0.00001 \quad (\text{B6})$$

$$\frac{V_{\text{sep}}}{V_{\text{phys}}} = 0.2424 \pm 0.0002. \quad (\text{B7})$$

The separable states only account for about a quarter of the state space in our volume measure, which is the Euclidean measure on M . This measure has the virtue that the distance between two different values of \vec{n} corresponds to a physical distance between 15 ‘‘pointers’’ if a complete measurement of all 15 observables is made. The volume in this measure is different from that of Ref. [39], where eigenvalues of the density matrix were used to discriminate states. With that approach the separable states occupy more than half the volume of the full state space.

A probability distribution function $P(C)$ for various $|\vec{n}|$ can be computed in a similar way. This is shown in Fig. 11. Again, appreciable entanglement is concentrated at a fairly specific radius. At $|\vec{n}| = \sqrt{3}$, i.e., for all pure states, the measure of separable states is zero. This is because pure separable states are parametrized by 4 parameters while pure states require 6 parameters. As stated above, S contains a ball of radius $|\vec{n}| = 1/\sqrt{3} \simeq 0.57735$. The numerical study indicates that the maximum radius is at about $|\vec{n}| \simeq 0.5782$. Although there is some angular variation in the function $C(\vec{n})$, the magnitude of \vec{n} is a good rough indicator for the entanglement.

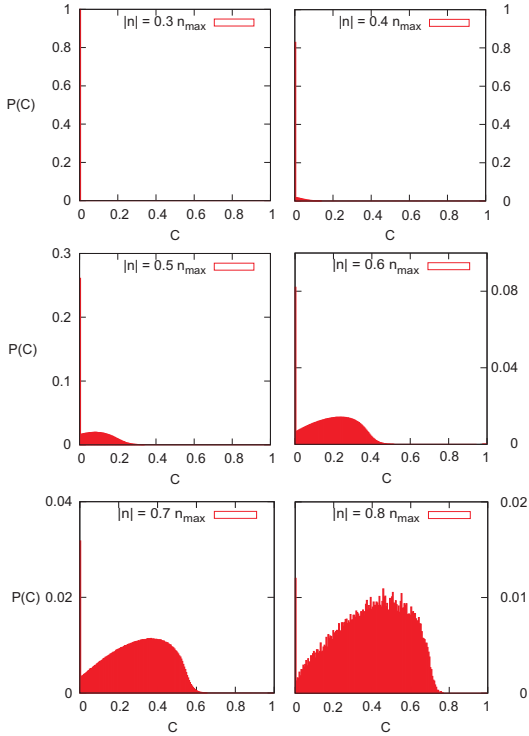


FIG. 11. Probability distribution of concurrence at different radius $|\tilde{n}|$. For small $|\tilde{n}|$, $P(C=0)$ is close to 1, i.e., almost all states \tilde{n} are separable. As $|\tilde{n}|$ increases, more and more states are entangled and the probability $P(C=0)$ keeps decreasing. $n_{\max} = \sqrt{3}$.

Appendix C: dynamical subspace D

In the text we defined the dynamical subspace D informally as the set of all trajectories allowed by the set of initial conditions and the equations of motion. Here we give a more formal definition.

The authors of a model generally specify n parameters in the total Hamiltonian for the coupled system and bath. These parameters vary over some ranges, $g_{1,\min} \leq g_1 \leq g_{1,\max}$, etc., giving a set $G = \{g_i\}$. Furthermore, a set of initial conditions is also given by a similar set H . For example, in the YE model, $G = \{\Gamma\}$ with $0 \leq \Gamma < \infty$, and $H = \{a_0\}$ with $0 \leq a_0 \leq 1$. In the literature, G and H are almost always manifolds (or manifolds with boundaries), as they are in this example. Finally $T = \{t\}$ with $0 \leq t < \infty$ is always a 1-manifold. The equations of motion then define a smooth map $N : G \times H \times T \rightarrow M$, where M is the state space. The dynamical subspace D is then defined as $D = \text{Image}(N)$.

ACKNOWLEDGMENTS

We thank Amrit De, Alex Lang and Andre L. Saraiva for helpful discussions. This work was supported by Grant NSF-ECS-0524253 and NSF-DMR-0805045, by the DARPA QuEST program, and by ARO and LPS Grant W911NF-08-1-0482.

-
- [1] R. Horodecki, P. Horodecki, M. Horodecki, and K. Horodecki, *Rev. Mod. Phys.* **81**, 865 (Jun 2009).
 - [2] M. A. Nielsen and I. L. Chuang, *Quantum Computation and Quantum Information*, 1st ed. (Cambridge University Press, 2000).
 - [3] S. Hill and W. K. Wootters, *Phys. Rev. Lett.* **78**, 5022 (Jun 1997); W. K. Wootters, *ibid.* **80**, 2245 (Mar 1998); *Quantum Information and Computation* **1**, 27 (2001).
 - [4] T. Yu and J. H. Eberly, *Science* **323**, 598 (2009).
 - [5] M. P. Almeida, F. de Melo, M. Hor-Meyll, A. Salles, S. P. Walborn, P. H. S. Ribeiro, and L. Davidovich, *Science* **316**, 579 (2007); J. Laurat, K. S. Choi, H. Deng, C. W. Chou, and H. J. Kimble, *Phys. Rev. Lett.* **99**, 180504 (Nov 2007); J.-S. Xu, C.-F. Li, M. Gong, X.-B. Zou, C.-H. Shi, G. Chen, and G.-C. Guo, **104**, 100502 (Mar 2010).
 - [6] K. Życzkowski, P. Horodecki, M. Horodecki, and R. Horodecki, *Phys. Rev. A* **65**, 012101 (Dec 2001).
 - [7] T. Yu and J. H. Eberly, *Phys. Rev. Lett.* **93**, 140404 (Sep 2004).
 - [8] T. Yu and J. H. Eberly, *Phys. Rev. Lett.* **97**, 140403 (Oct 2006); T. Yu and J. Eberly, *Optics Communications* **264**, 393 (2006); **283**, 676 (2010).
 - [9] J.-H. Huang and S.-Y. Zhu, *Phys. Rev. A* **76**, 062322 (Dec 2007).
 - [10] X. Cao and H. Zheng, *Phys. Rev. A* **77**, 022320 (Feb 2008).
 - [11] A. Al-Qasimi and D. F. V. James, *Phys. Rev. A* **77**, 012117 (Jan 2008).
 - [12] M. Hernandez and M. Orszag, *Phys. Rev. A* **78**, 042114 (Oct 2008).
 - [13] K. Roszak, P. Horodecki, and R. Horodecki, *Phys. Rev. A* **81**, 042308 (Apr 2010).
 - [14] M. Al-Amri, G.-x. Li, R. Tan, and M. S. Zubairy, *Phys. Rev. A* **80**, 022314 (Aug 2009).
 - [15] M. Ikram, F.-l. Li, and M. S. Zubairy, *Phys. Rev. A* **75**, 062336 (Jun 2007).
 - [16] A. Vaglica and G. Vetri, *Phys. Rev. A* **75**, 062120 (Jun 2007).
 - [17] J. León and C. Sabín, *Phys. Rev. A* **79**, 012301 (Jan 2009).
 - [18] B. Bellomo, R. Lo Franco, and G. Compagno, *Phys. Rev. Lett.* **99**, 160502 (Oct 2007); *Phys. Rev. A* **77**, 032342 (Mar 2008).
 - [19] D. Zhou, A. Lang, and R. Joynt, *Quant. Info. Processing* **9**, 727 (March 2010).
 - [20] Z. Ficek and R. Tanaś, *Phys. Rev. A* **74**, 024304 (Aug 2006); L. Mazzola, S. Maniscalco, J. Piilo, K.-A. Suominen, and B. M. Garraway, **79**, 042302 (Apr 2009); C. E. López, G. Romero, F. Lastra, E. Solano, and J. C. Retamal, *Phys. Rev. Lett.* **101**, 080503 (Aug 2008).
 - [21] M. Yönaç, T. Yu, and J. H. Eberly, *Journal of Physics B* **39**, S621 (2006); M. Yönaç and J. H. Eberly, *Opt. Lett.* **33**, 270 (2008).

- [22] K. Ann and G. Jaeger, Phys. Rev. A **76**, 044101 (Oct 2007).
- [23] Y. S. Weinstein, Phys. Rev. A **79**, 012318 (Jan 2009); **79**, 052325 (May 2009); **80**, 022310 (Aug 2009).
- [24] L. Aolita, R. Chaves, D. Cavalcanti, A. Acín, and L. Davidovich, Phys. Rev. Lett. **100**, 080501 (Feb 2008).
- [25] C.-Y. Lai, J.-T. Hung, C.-Y. Mou, and P. Chen, Phys. Rev. B **77**, 205419 (May 2008).
- [26] J. P. Paz and A. J. Roncaglia, Phys. Rev. Lett. **100**, 220401 (Jun 2008); Phys. Rev. A **79**, 032102 (Mar 2009).
- [27] S.-Y. Lin, C.-H. Chou, and B. L. Hu, Phys. Rev. D **78**, 125025 (Dec 2008).
- [28] R. Vasile, S. Olivares, M. G. A. Paris, and S. Maniscalco, Phys. Rev. A **80**, 062324 (Dec 2009).
- [29] G. Kimura, Physics Letters A **314**, 339 (2003); M. S. Byrd and N. Khaneja, Phys. Rev. A **68**, 062322 (Dec 2003).
- [30] G. Mahler and R. Wawer, *Quantum Networks: Dynamics of Open Nanostructures*, 2nd ed. (Springer, 1998).
- [31] R. Alicki and K. Lendi, *Quantum dynamical semigroups and applications* (Springer-Verlag, 1987).
- [32] R. Joynt, D. Zhou, and Q.-H. Wang, Int. J. Mod. B **25**, 2115 (2011).
- [33] M. S. Byrd, C. A. Bishop, and Y.-C. Ou, Phys. Rev. A **83**, 012301 (Jan 2011).
- [34] J. M. Chow, L. DiCarlo, J. M. Gambetta, A. Nunnenkamp, L. S. Bishop, L. Frunzio, M. H. Devoret, S. M. Girvin, and R. J. Schoelkopf, Phys. Rev. A **81**, 062325 (Jun 2010).
- [35] L. DiCarlo, M. Reed, L. Sun, B. Johnson, J. Chow, J. Gambetta, L. Frunzio, S. Girvin, M. Devoret, and R. Schoelkopf, Nature **467**, 574 (2010).
- [36] R. A. Horn and C. R. Johnson, *Matrix analysis / Roger A. Horn, Charles R. Johnson* (Cambridge University Press, New York, 1985).
- [37] L. Jakbczyk and M. Siennicki, Physics Letters A **286**, 383 (2001).
- [38] A. R. P. Rau, Journal of Physics A: Mathematical and Theoretical **42**, 412002 (2009).
- [39] K. Zyczkowski, P. Horodecki, A. Sanpera, and M. Lewenstein, Phys. Rev. A **58**, 883 (Aug 1998).
- [40] J. Munkres, *Topology: a first course* (Prentice-Hall, 1974).
- [41] R. F. Werner, Phys. Rev. A **40**, 4277 (Oct 1989).
- [42] D. Zhou and R. Joynt(2010), arXiv:1006.5474 [quant-ph].
- [43] A. De, A. Lang, D. Zhou, and R. Joynt, Phys. Rev. A **83**, 042331 (Apr 2011).
- [44] J. Preskill, “Ph219 lecture notes,” <http://www.theory.caltech.edu/people/preskill/ph229/>.
- [45] T. Yu and J. H. Eberly, Quantum Inform. Comput. **7**, 459 (2007).
- [46] S. Kogan, *Electronic Noise and Fluctuations in Solids* (Cambridge University Press, 2008).
- [47] R. C. Bialczak, R. McDermott, M. Ansmann, M. Hofheinz, N. Katz, E. Lucero, M. Neeley, A. D. O’Connell, H. Wang, A. N. Cleland, and J. M. Martinis, Phys. Rev. Lett. **99**, 187006 (Nov 2007).
- [48] J. Bergli, Y. M. Galperin, and B. L. Altshuler, New Journal of Physics **11**, 025002 (2009).
- [49] B. Cheng, Q.-H. Wang, and R. Joynt, Phys. Rev. A **78**, 022313 (Aug 2008); D. Zhou and R. Joynt, **81**, 010103 (Jan 2010).
- [50] M. J. Testolin, J. H. Cole, and L. C. L. Hollenberg, Phys. Rev. A **80**, 042326 (Oct 2009).
- [51] L. Gurvits and H. Barnum, Phys. Rev. A **68**, 042312 (Oct 2003); **72**, 032322 (Sep 2005).
- [52] K. Kraus, *States, effects, and operations : fundamental notions of quantum theory* (Springer-Verlag, 1983).
- [53] V. Guillemin and A. Pollack, *Differential topology* (Prentice-Hall, 1974).
- [54] G. Watson, *Statistics on Spheres* (Wiley, New York, 1983).